Chemical Science

ROYAL SOCIETY OF CHEMISTRY

EDGE ARTICLE

View Article Online
View Journal | View Issue

Cite this: *Chem. Sci.*, 2025, **16**, 17461

All publication charges for this article have been paid for by the Royal Society of Chemistry

Received 25th June 2025
Accepted 21st August 2025

DOI: 10.1039/d5sc04670j

rsc.li/chemical-science

Atomic insights into how electrolyte concentration controls CO electroreduction to acetate

Xiaowan Bai, [ab] Lin Jiang [ab] and Yan Jiao *[ab]

During the electrochemical conversion of CO to acetate on copper-based catalysts, the electrolyte concentration plays a crucial role in acetate selectivity. However, the correlation between the electrolyte concentration and the local microenvironment as well as the reaction kinetics remains unclear. In this work, we report for the first time the impact of KOH concentration on the solvent structure and reaction kinetics for CO reduction to acetate using advanced *operando* computational methods. With increasing KOH concentration, we find that the interfacial solvent structure becomes dense and the hydrogen bond network becomes more stable which benefits the directional transfer of protons/hydroxides. In terms of reaction kinetics, high-concentration KOH not only promotes the generation of *OH, but also accelerates its combination with surface *CO to form *COOH, a key step in the production of acetate. These insights offer a practical strategy for tuning electrolytes to boost catalyst performance.

1 Introduction

The electrochemical conversion of carbon dioxide (CO_2) into value-added chemicals and fuels using renewable electricity is an attractive strategy to achieve carbon-neutral sustainable development and mitigate climate change caused by the excessive demand for fossil fuels.[1–3] Among the products of CO_2 electroreduction, carbon monoxide (CO) is one of the most economically feasible intermediates due to its high selectivity of up to 99%.[2,4–6] Utilizing CO directly as a reactant can significantly enhance C–C coupling reaction, enabling the efficient synthesis of multi-carbon products (C_n, $n \geq 2$).[7–11] Therefore, the electrochemical CO reduction reaction (CORR) has emerged as a key technology for the efficient conversion of CO_2 into high-value-added chemicals *via* a cascade pathway ($CO_2 \rightarrow CO \rightarrow C_n$).[12,13]

For multi-carbon products, acetate is highly desired since it is a raw material for many important industrial products and has a large market demand.[1,14–16] Under highly alkaline conditions, high selectivity for acetate is usually achieved, which is higher than the faradaic efficiency (<5%) in CO_2 reduction.[17,18] This can be attributed to several important factors. Firstly, the increased coverage of *CO as a key intermediate promotes the C–C coupling step, which improves acetate selectivity.[19] Secondly, at high concentrations of alkaline electrolytes, OH^- near the electrode–electrolyte interface can be used as a reactant in the process of acetate production.[20] In addition, mass transport can control the competition between the desorption and the further reduction of stable intermediates with a corresponding impact on selectivity.[21] It is worth noting that all of these factors are closely related to the local microenvironment at the electrode–electrolyte interface. Although some studies have reported the relationship between the local microenvironment and performance in CO_2RR,[7,22,23] an in-depth understanding of the effect of the local microenvironment on reaction kinetics in CORR is still lacking at the atomic level.

In terms of the reaction mechanism, it has been proposed that the formation of acetate is a nucleophilic reaction of OH^- directly attacking adsorbed ketene (*H_2CCO or other early intermediates).[17,20,24] Electrostatic repulsion and the limited accessibility of OH^- near the intermediates make this step seem unlikely. Subsequently, Chan *et al.* proposed that acetate formation occurs *via* a solution-phase reaction after C–C coupling,[21] but it is still difficult to explain the selectivity of ethylene and acetate.[25] Given these findings, we have proposed a new mechanism for explaining acetate formation in CORR that is consistent with experimental results and we find that prioritized coupling between adsorbed *CO and *OH is a key step.[25] Very recently, Yeo *et al.* verified the feasibility of our proposed mechanism.[26] However, the issues regarding the source of *OH and the increase in acetate yields with increasing concentration of alkaline electrolyte have not been resolved.

Here, we explore the effects of different KOH concentrations on the local microenvironment at the electrode–electrolyte interface, proton or hydroxide transfer, and the reaction kinetics of key steps under working conditions. A "constant-potential hybrid solvation-dynamic model" (CP-HS-DM) is implemented to investigate in detail the changes in the dynamic surface charge and local microstructure with varying KOH concentrations to obtain more detailed kinetic

[a]*School of Chemical Engineering, The University of Adelaide, Adelaide, SA 5005, Australia. E-mail: yan.jiao@adelaide.edu.au*

[b]*ARC Centre of Excellence for Carbon Science and Innovation, Australia*

information. Different KOH concentrations include one K^+ with F^- (KF), one K^+ with one OH^- (KOH), and two K^+ with two OH^- (2KOH). The results reveal that a high KOH concentration can enhance the stability of the solvent structure. It is due to the increased coordination number of cations with the surrounding water molecules and the weak hydrogen bonding provided by OH^- in the solution. Furthermore, the surface charge is reduced and the electrostatic repulsion is weakened compared to the KF and KOH environment, resulting in preferential adsorption of an $*H_2O$ molecule and OH^- closer to the surface. Under this condition, $*H_2O$ spontaneously undergoes deprotonation, and H^+ is transported through the water network to the solution to form H_2O with one OH^-, resulting in one *OH remaining on the surface. Classical molecular dynamics simulations are employed to further elucidate the microstructural evolution in the diffusion layer. The results show that higher KOH concentrations extend the hydrogen bond lifetimes, leading to a more stable hydrogen-bond network that promotes directional proton transfer. We also evaluated the kinetic barriers for key steps at different KOH concentrations, including proton transport in solution, *CO dimerization, and the coupling of *CO with surface *OH. At higher KOH concentrations, all of these kinetic barriers are reduced. Therefore, this work not only reveals the influence of electrolyte concentration on the local microenvironment and the regulation of reaction kinetics in key steps, but also provides theoretical guidance for the rational design of electrocatalytic systems to further improve acetate selectivity.

2 Theoretical methods

All periodic density functional theory (DFT) calculations were carried out using the Vienna *ab initio* simulation package (VASP)[27,28] with the projector-augmented-wave (PAW) method.[29,30] The generalized gradient approximation (GGA) framework with the Perdew–Burke–Ernzerhof (PBE) functional was used to describe electron exchange–correlation interactions.[31] Empirical Grimme's D3 method[32] was adopted to account for van der Waals (vdW) forces to liquid water solvents. *Ab initio* molecular dynamics (AIMD) simulations were performed to investigate the dynamic effects of different electrolyte concentrations on the local microenvironment at the electrode–electrolyte interface during CO reduction to acetate. The slow-growth (SG) approach[33,34] was employed to obtain free energy profiles, providing information on mass transport and reaction kinetics of key reaction steps. Both AIMD and SG are embedded in a constant-potential hybrid solvation-dynamic model (CP-HSDM) to fully account for the effects of surface charge and explicit solvents.[35,36] The cutoff energy was set to 400 eV. The canonical ensemble condition (NVT) was used through a Nosé–Hoover thermostat[37] set at 300 K with a time step of 0.5 fs. The gamma point of the Brillouin zone was considered in all AIMD simulations. An applied potential of −0.65 V (*vs.* RHE) based on experimental conditions[12,38] was preset for the equilibrium AIMD simulations and free energy computations.

A four-layer 4 × 4 Cu(100) surface was constructed with the two bottom layers fixed. Explicit water molecules ($39H_2O$) were introduced on the Cu(100) surface to simulate the aqueous solution environment. The simulation cell size of the Cu–water interfacial models was 10.22 Å × 10.22 Å × 30 Å, where a ∼10 Å vacuum region in the *Z*-direction was added to avoid periodic effects. Two CO molecules were adsorbed on the surface to explore the reaction kinetics of key steps. To investigate the effect of different local concentrations on the performance of CO reduction to acetate, three different electrolyte environments were considered, including KF, KOH, and 2KOH. The calculation details of classical molecular dynamics and other details are described in the SI.

3 Results and discussion

Fig. 1a illustrates the performance of CO reduction to acetate at varying KOH concentrations reported in several recent experimental studies.[1,12,17,19,39,40] A clear trend is observed in which the faradaic efficiency (FE) of acetate increases with increasing KOH concentration. A recent study has shown that high *OH coverages confine CO adsorption to a bridge configuration.[26] In the meantime, they verified that the reaction mechanism we proposed is feasible through DFT simulations. This provides a deeper understanding of the complex reaction mechanisms involved in the formation of acetate. However, the clarification of the reaction mechanism alone is not enough to explain the trend in Fig. 1a, because the microenvironment and reaction mechanism are equally important in influencing the overall performance. Therefore, we constructed three Cu(100)/electrolyte interface models to explore the effects of different KOH concentrations on the microenvironment and reaction kinetics, as shown in Fig. 1b.

3.1 Assessing stability

The stability of the structure is critical for the evaluation of proton transport and reaction kinetics. To obtain the response of the microenvironment to different KOH concentrations at the electrode–electrolyte interface, we constructed three interface models with nearly identical cation and anion heights on the Cu(100) surface and equilibrated them for up to 20 ps at −0.65 V *vs.* RHE, as shown in Fig. S1 and S2. The radial distribution function (RDF) of the oxygen–hydrogen of liquid water was obtained from the last 2.0 ps of the AIMD equilibrium trajectory (Fig. S3). It was found that the positions of the first, second and third maximum for the three systems studied are 0.95, 1.75 and 3.15 Å, respectively. This is consistent with previous experimental and theoretical results,[41,42] demonstrating that the solvent structure is stable, but the differences in solvent structure between the three concentrations were not clearly distinguished. Therefore, we compared the ensemble similarity of 4000 structures using Jensen–Shannon divergence (JSD) in Fig. 2a–c.[43] Structurally, all curves eventually converge to zero, but as the KOH concentration increases, the trajectories of the K^+ ions drop to low ensemble divergence faster, indicating that the conformation can cover the same region of conformational space as the entire 2.0 ps simulation sooner. Root-mean-square deviation (RMSD) is another measure used

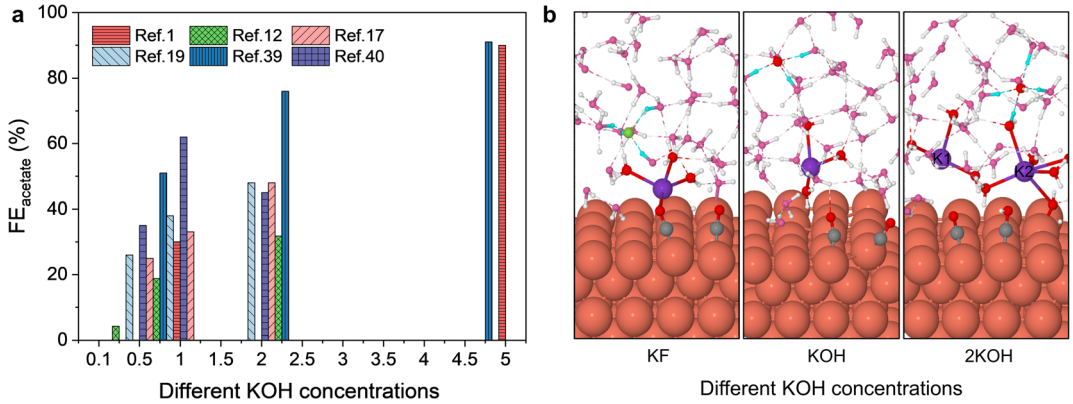

Fig. 1 Electroreduction of CO to acetate on Cu-based catalysts. (a) The experiments determined the faradaic efficiency of the acetate product as a function of KOH concentration on Cu-based catalysts. Data from ref. 1, 12, 17, 19, 39 and 40. (b) Well-equilibrated interface models at different KOH concentrations including one K^+ with one F^-, one K^+ with one OH^-, and two K^+ with two OH^-. The orange, pink, white, gray, green, and purple spheres represent Cu, O, H, C, F, and K atoms, respectively. The red and cyan spheres represent O atoms in H_2O coordinated with K ions and hydrogen atoms forming hydrogen bonds with F^- or OH^-, respectively.

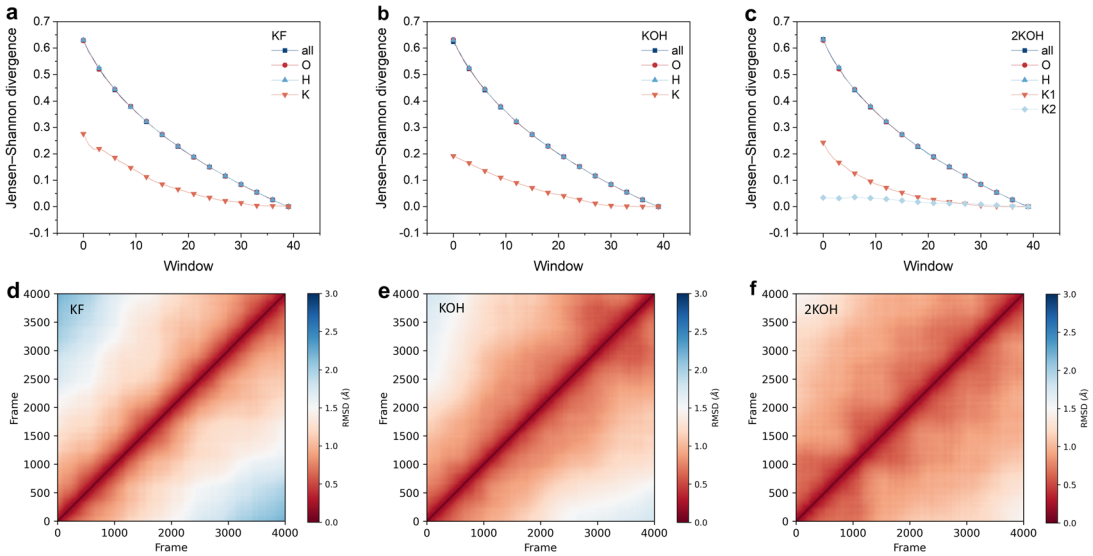

Fig. 2 Stability assessment of the three studied systems. (a)–(c) Jensen–Shannon divergence of all atoms, O, H, and K atoms over the last 2.0 ps (equivalent to 4000 frames) of the AIMD simulation trajectories for the KF, KOH, and 2KOH interface models at $U = -0.65$ V *vs.* RHE. The window is set to 100. (d)–(f) Pairwise RMSD of all atoms in the KF, KOH, and 2KOH interface models.

to track conformational changes and evaluate stability relative to the initial structure during simulation, where a lower value indicates a more similar structure.[44] Fig. S4 shows the RMSD changes of all atoms, oxygen atoms, hydrogen atoms, and K^+ ions at KF, KOH, and 2KOH concentrations compared to their initial conformations, revealing that the solvent structure is most stabilized at the 2KOH concentration with the smallest RMSD value, which is consistent with the JSD observation. However, RMSD only captures the overall deviation of atomic positions with varying simulation time and ignores the detailed arrangement or local conformation. Two structures with the same RMSD can differ significantly in shape due to local distortions, rotations, or rearrangements. RMSD alone may mislead our judgment of structural similarity. Therefore, to more accurately assess the global convergence of the simulations, pairwise RMSD[45,46] between each snapshot was considered. Comparing the three studied systems, we found that as the KOH concentration increases, the blue region decreases and the red region increases, as shown in Fig. 2d–f and S5–S7. These results indicate that more similar conformations are generated during equilibration at higher KOH concentrations. Therefore, the local microstructure is indeed most stable at the 2KOH concentration.

3.2 analysis

To understand the reason for the solvent structure stability at high KOH concentration, a statistical analysis of the coordination of K^+ and F^-/OH^- ions with surrounding water molecules was performed through the RDF and coordination number (CN)

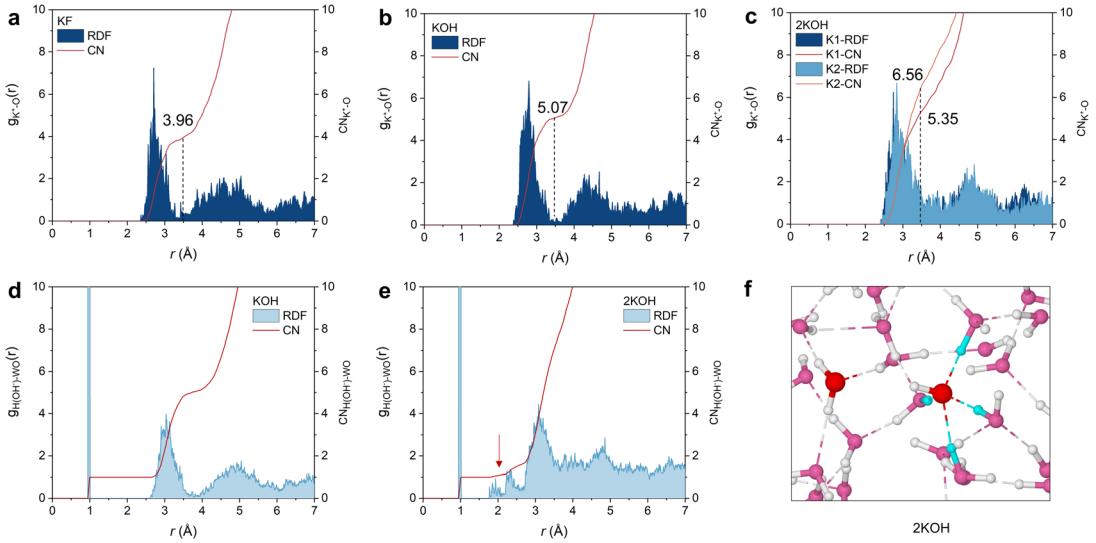

Fig. 3 Local microenvironmental analysis of three interface systems. The radial pair distribution function (g_{K^+-O}) and coordination number (CN_{K^+-O}) between K^+ and oxygen atoms in water molecules and *CO in (a) KF, (b) KOH, and (c) 2KOH interfacial models. The radial pair distribution function between the hydrogen atom of OH^- and the oxygen atom of water molecules at (d) KOH and (e) 2KOH concentrations. (f) Local solvent structure in the 2KOH system.

obtained by integrating the RDF, as shown in Fig. 3. In the first solvation shell, the number of O atoms surrounding the cation (including O atoms of H_2O and *CO) increases with increasing KOH concentration(Fig. 3a–c), while the number of H atoms in the water molecules surrounding the anion (F^- and OH^-) is equal to four (Fig. S8). Notably, we observed that the hydrogen of OH^- occasionally approaches the oxygen of a water molecule to form a weak hydrogen bond at a distance of about 2.0 Å from the H atom of OH^- at 2KOH concentration (Fig. 3e and f). This phenomenon was not observed at the KOH concentration (Fig. 3d). Therefore, the synergistic effect of the high O coordination number surrounding the cation and the weak hydrogen bond provided by OH^- results in a more stable solvent structure under 2KOH than under KF and KOH conditions.

Next, we turn our attention to the effect of different KOH concentrations on the interfacial water structure. The density distributions of hydrogen and oxygen atoms of water molecules along the *Z*-direction at different KOH concentrations are shown in Fig. 4a and b. For hydrogen atoms, the first distinct peak appears at 2.0 Å from the surface and becomes sharper with increasing KOH concentration. For oxygen atoms, the position of the peak shifts toward the surface as the KOH concentration increases. Specifically, the first peak appears at 1.8 Å at 2KOH concentration, with very low intensity, which is attributed to the fact that only the O-terminus of one *OH is chemisorbed. The second and third peaks exhibit the highest density distribution of oxygen atoms at 2.7 and 3.0 Å, respectively, corresponding to non-chemisorbed water molecules. However, for both KF and KOH, only one highest peak occurs at 2.7 Å, indicating that the interfacial water concentration is less than that of 2KOH. Meanwhile, we observed that the solvent structure in the *Z* direction became more compressed with increasing KOH concentration, from 16 Å to 14 Å (Fig. 4b), indicating that the solvent structure of the electric double layer at the interface is denser.[47]

In addition, we calculated the total average cosine (ϕ) distribution curve based on AIMD trajectories with a width of 0.2 Å along the *Z* direction and analyzed the orientation of water molecules at the interface at different KOH concentrations (Fig. 4c). Here, ϕ is the angle between the water bisector ($\tilde{b}$) and the surface normal ($\tilde{n}$) of the water molecule. $\phi < 90$, and $\cos(\phi) > 0$, which means that the water molecules are arranged in an O-down configuration. In contrast, for $\phi > 90$ and $\cos(\phi) < 0$, the water molecules are arranged in an H-down configuration as shown in Fig. S9. Within a range of about 2.7 Å from the first layer of the Cu surface, the number of interfacial water molecules in the O-down configuration increases with increasing KOH concentration. This is caused by a reduction in the number of negative charges on the surface and the weakening of the electrostatic repulsion, as shown in Fig. 4d. Therefore, the OH^- under the 2KOH condition is closer to the surface than under the KOH concentration. For the KF condition, since F^- has strong hydration with surrounding water molecules, it exhibits lower mobility in aqueous solution and therefore keeps moving near the initial position as shown in Fig. S10. In the region of 2.7 Å < *Z* < 16 Å from the surface, the interfacial water in the KF environment alternates between O-down and H-down orientations along the *Z*-direction, which suggests that the interfacial water is disordered, resulting in a more relaxed solvent structure.[48] In contrast, in the region of 6.5 Å < *Z* < 12 Å from the surface, the O-down orientation predominates in the KOH environment, while the region from 12 to 15 Å is dominated by the H-down orientation. At the 2KOH concentration, the O-down dominated interfacial water distribution is further towards the surface, located in the range of about 4.0 to 9.0 Å, while H-down predominates in the range of 11 to 14.5 Å.

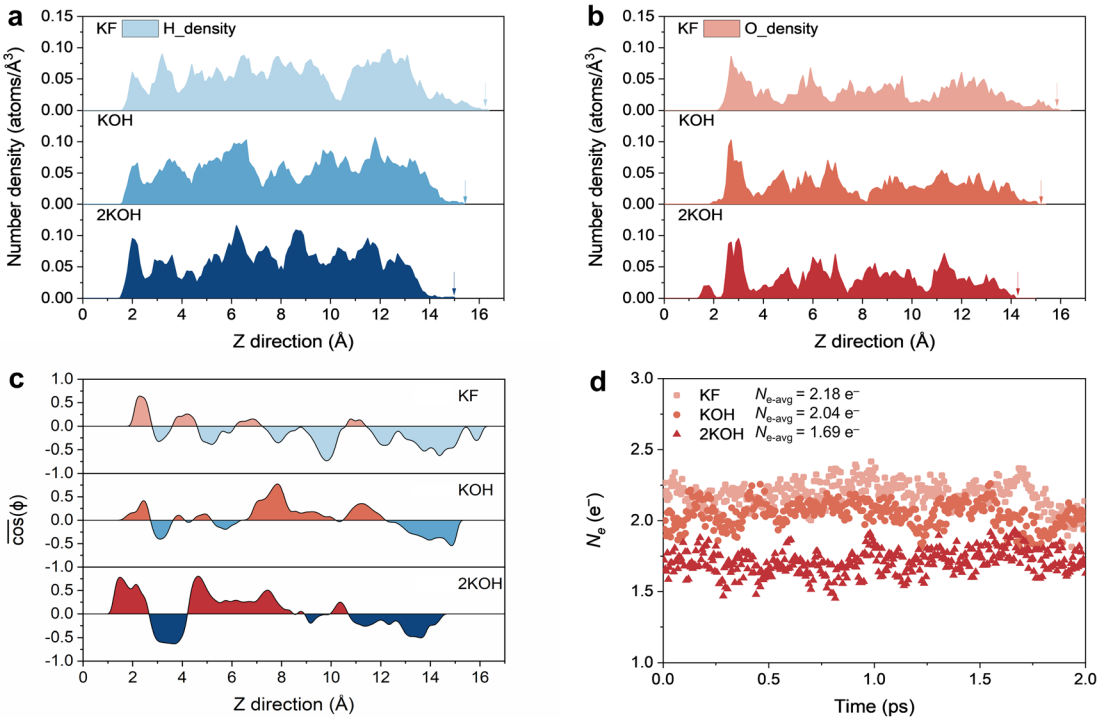

Fig. 4 The effect of different KOH concentrations on the interfacial water structure. Distribution of number densities of (a) hydrogen and (b) oxygen atoms at different KOH concentrations along the surface normal direction during the last 2.0 ps equilibration. (c) Distribution profiles of the angle (ϕ) formed between the water bisector ($\tilde{b}$) and the surface normal direction ($\tilde{n}$). (d) Dynamic evolution of the net electron (N_e) during the last 2.0 ps of AIMD simulation of at $U_{RHE} = -0.65$ V.

Therefore, as the KOH concentration increases, the arrangement of interfacial water molecules tends to be more orderly, making the solvation structure of the electric double layer denser, which may be beneficial for transfer of hydrogen or hydroxide.

3.3 Solvent structure in the diffuse layers

The above section analyzed the solvent structure near the electrode surface. Next, we will study the effect of different KOH concentrations on the solvent structure in the diffuse layer. This is because the hydrogen bond network structure of solvent molecules, proton transfer behavior, and the local distribution of ions in the diffuse layer undergo significant changes with electrolyte concentration, thereby affecting the reaction behavior at the interface. We constructed 1 M KF, 1 M KOH, 2 M KOH and 5 M KOH bulk phase solvent models shown in Fig. 5a, S11 and Table S2. The radial distribution functions (RDFs) for K^+–WO (O of water) and F^-/OH^-–WO are shown in Fig. 5b and c. Our results show the first peaks at approximately 2.80 and 2.72 Å for K^+–WO and OH^-–WO, respectively, which is consistent with previous study results.[49] As the electrolyte concentration increases, the coordination number of K^+–H_2O, OH^-–H_2O and H_2O–H_2O decreases (Fig. S12 and S13). We further analyzed the mean square displacement (MSD) as a function of time and the self-diffusion coefficients of K^+ and OH^- at different KOH concentrations (Fig. 5d and S14). With increasing KOH concentration, the self-diffusion coefficients of K^+ and OH^- decreased significantly, indicating that the solvent structure is more stable, which leads to restricted migration of ions. To further reveal the microscopic mechanism underlying the stability of the solvent structure, we analyzed the intermolecular interactions of the systems from the perspective of hydrogen bonding. Fig. 5e, f and S15 show the number and lifetime of hydrogen bonds between F^-/OH^-–H_2O and H_2O–H_2O at different KOH concentrations. The results show that as the KOH concentration increases, the number of hydrogen bonds decreases slightly, but the lifetime of the hydrogen bonds is extended, indicating that the hydrogen bond network tends to be stable over a short period of time, which is conducive to the directional transfer of protons or hydroxide. This is consistent with the influence of the solvent structure near the surface.

3.4 Assessing reaction kinetics

The above results reveal the evolution trend of the solvent structure in the diffuse layer at different KOH concentrations. Next, we evaluate the effect of different KOH concentrations on H^+/OH^- transfer kinetics at the electrode–electrolyte interface. As shown in Fig. 6a and S16–S18, we set up five, five, and four pathways to calculate the kinetic barriers for the transport of OH^- ions from the solution to the Cu surface of the first layer in KF, KOH, and 2KOH environments, respectively. There are only four pathways at 2KOH concentration as shown in Fig. 6b because OH^- is located near the surface as mentioned above,

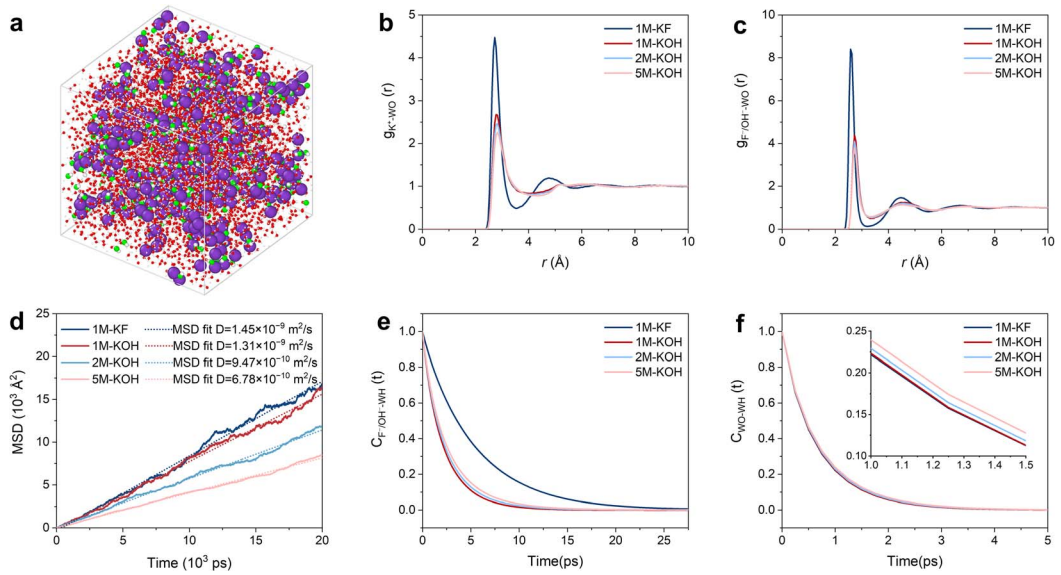

Fig. 5 Solvent structure analysis in the diffusion layer. (a) Molecular dynamics snapshot of 5 M KOH in an aqueous solution. The purple, green and white spheres represent the K^+, the O atom in OH^-, and the H atom in OH^-, respectively. The shrunken red and white spheres are the O and H of the H_2O molecule. RDF for (b) K^+–WO and (c) F^-/OH^-–WO as a function of KOH concentration. (d) Mean square displacements and the self-diffusion coefficients of K^+ as a function of KOH concentration. Hydrogen bond lifetime of (e) F^-/OH^-–WH and (f) WO–WH calculated from MD simulations.

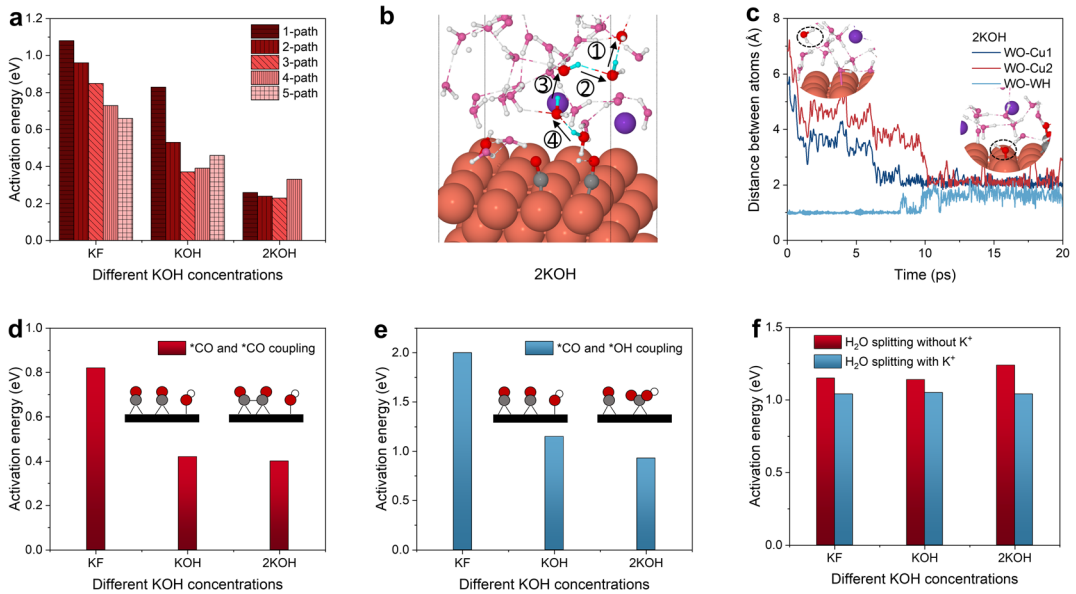

Fig. 6 The effect of different KOH concentrations on reaction kinetics. (a) OH^- transfer barriers in the KF, KOH, and 2KOH interface models. (b) The OH^- transfer roadmap under the 2KOH interface model. Among them (1), (1)+(2), (1)+(2)+(3), and (1)+(2)+(3)+(4) correspond to 1-path, 2-path, 3-path and 4-path in (a), respectively. (c) The distance evolution of OH^- from the ion to the adsorption process during the 20 ps equilibrium. Calculated activation energies for the (d) *CO and *CO coupling step, (e) *CO and *OH coupling step, and (f) HER-Volmer step in three interface models.

and four H-transfers are sufficient for the formation of surface OH^-. The distance between the transferred H^+ and O atoms along the longest reaction path for each model is summarized in Fig. S19. Under the KF condition, H^+ is transferred to the solution to form H_3O^+ because the bond lengths of H_4–O_4 and H_5–O_5 do not converge to ~0.96 Å, whereas H^+ is transferred to OH^- in solution to form water under KOH and 2KOH conditions. The results obtained by the SG method showed that the barriers for H^+ transfer from water molecules to the solution follow the order KF > KOH > 2KOH, indicating that mass transport of H^+ is the most difficult at the KF concentration as shown in Fig. 6a. It is worth noting that one water molecule

preferentially adsorbs on the surface during structural equilibration and spontaneously splits into one *OH and H^+ at 10 ps at the 2KOH concentration, and then H^+ is quickly transferred to the solution through the water structure to combine with OH^- to form H_2O as shown in Fig. 6c. This results in one OH^- remaining adsorbed on the surface, while the other OH^- stays in solution as the initial structure for the calculated H^+ transport at a 2KOH concentration. Therefore, the increase in OH^- concentration at the electrode–electrolyte interface can promote the deprotonation of H_2O, reduce the barrier for forming surface OH^- or *OH, and provide a fast channel for the transfer of OH^- from solution to the catalyst surface.

As mentioned in our previous work on the CO reduction to acetate, high CO pressure can induce coupling of *CO with surface *OH, producing *COOH, opening the pathway for the formation of acetate.[25] Recently, this mechanism has also been verified to be feasible.[26] Therefore, we evaluated the competition between *CO–*CO coupling and *CO–*OH coupling at different KOH concentrations as shown in Fig. 6d, e and S20–S23. Under the KF condition, the solution is OH^--free and thus the adsorbed H_2O molecules react with *CO, whereas *OH couples with *CO under KOH and 2KOH conditions. The kinetic barriers for both reactions decrease with increasing KOH concentration. The barrier for *CO and *CO coupling is lower than that for the formation of *COOH by the coupling of *CO with *OH, which is due to the fact that the presence of *OH promotes the dimerization of *CO.[50] Although *CO and *CO coupling is favorable, the barrier for *CO–*OH coupling is further reduced when more *OH and *CO species are adsorbed on the surface.[25]

We also considered the Volmer step of the HER that competes with CO reduction as shown in Fig. 6f and S24–S26. We chose two interfacial water molecules, one coordinated to K^+ and the other uncoordinated. We found that the barriers for water splitting are greater than 1.00 eV, and the kinetic barrier for HER does not show significant changes at different KOH concentrations, which is consistent with the experimental results.[19] This may be attributed to the surface charge and density of the solution structure. For example, under the KF condition, the more negative surface charges lead to an H-down configuration in the interfacial water molecules, but the water structure is loose, and the mass transport of H^+ is difficult, making the water splitting to form adsorbed *H difficult. Under the 2KOH condition, although the water structure is dense, it is more favorable for *OH adsorption, resulting in difficult *H adsorption. Therefore, based on the above results, it is suggested that the changes in the local microenvironment induced by different KOH concentrations are crucial for reaction kinetics in CORR.

4 Conclusions

In this study, we revealed the effect of electrolyte concentration on the local microenvironment and reaction kinetics using *ab initio* molecular dynamics simulations under constant electrode potential as well as effective analytical methods. We demonstrated that the water molecules near the electrode–electrolyte interface become ordered and the solvent structure changes from loose to dense with increasing KOH concentration, due to the increased coordination of K^+ ions with the O atoms of the surrounding water molecules and the weak hydrogen bonding provided by OH^-. To further elucidate microstructural evolution in the diffusion layer, we performed classical molecular dynamics simulations. We found that an increase in KOH concentration can extend the hydrogen bond lifetimes of OH^-–H_2O and H_2O–H_2O, which is conducive to the directional proton transfer. The effect of electrolyte concentration on reaction kinetics was also explored at the electrode–electrolyte interface, including the proton transfer and the coupling of *CO and surface *OH. These kinetics became favorable with increasing KOH concentration, leading to a quick transfer of OH^- from solution to the catalyst surface and subsequent reaction with *CO, thus promoting high selectivity of CO reduction to acetate. Since OH^- transport and coverage are crucial for the formation of *COOH by *CO and *OH coupling, we believe that rationally designing the electrolyte and electrocatalyst structure to accelerate the rate of OH^- capture to form *OH on the surface and anchoring it around *CO would be an effective strategy to improve the yield of acetate. The interfacial electrolyte effects discussed here are not limited to acetate formation. Similar mechanisms are likely involved in CO reduction to other C_2^+ products such as ethylene and ethanol. This broader impact of electrolyte conditions on product selectivity presents an important direction for future studies.

Author contributions

Y. Jiao conceived the idea and supervised this work. X. W. Bai performed the DFT calculations and wrote the manuscript. L. Jiang provided the code for analysing the angle of water molecules. All authors discussed and analyzed the results during manuscript preparation.

Conflicts of interest

The authors declare no competing financial interest.

Data availability

The data supporting this article have been included as part of the SI: additional computational details, analytical methods and supplementary data and figures. The main contents include variations in energy, temperature, and atomic distances with time during AIMD simulations as well as activation energies calculated by the Slow-growth approach at constant potential. In addition, there are some results from LAMMPS simulations. See DOI: **https://doi.org/10.1039/d5sc04670j**.

Acknowledgements

The authors acknowledge financial support from the Australian Research Council (grant no. DE240100846, CE230100032 and DP250104259). Computations were supported by computational resources provided by the Australian Government

through NCI under the National Computational Merit Allocation Scheme, the Pawsey Supercomputing Research Centre with funding from the Australian Government and the Government of Western Australia, and the Phoenix High-Performance Computing (HPC) Service at The University of Adelaide.

References

1 S. Guo, Y. Liu, Y. Huang, H. Wang, E. Murphy, L. Delafontaine, J. L. Chen, I. V. Zenyuk and P. Atanassov, Promoting Electrolysis of Carbon Monoxide toward Acetate and 1-Propanol in Flow Electrolyzer, *ACS Energy Lett.*, 2023, **8**, 935–942.

2 S. Nitopi, E. Bertheussen, S. B. Scott, X. Liu, A. K. Engstfeld, S. Horch, B. Seger, I. E. L. Stephens, K. Chan, C. Hahn, J. K. Nørskov, T. F. Jaramillo and I. Chorkendorff, Progress and Perspectives of Electrochemical CO_2 Reduction on Copper in Aqueous Electrolyte, *Chem. Rev.*, 2019, **119**, 7610–7672.

3 X. She, L. Zhai, Y. Wang, P. Xiong, M. M.-J. Li, T.-S. Wu, M. C. Wong, X. Guo, Z. Xu, H. Li, H. Xu, Y. Zhu, S. C. E. Tsang and S. P. Lau, Pure-water-fed, electrocatalytic CO_2 reduction to ethylene beyond 1,000 h stability at 10 A, *Nat. Energy*, 2024, **9**, 81–91.

4 M. P. L. Kang, M. J. Kolb, F. Calle-Vallejo and B. S. Yeo, The Role of Undercoordinated Sites on Zinc Electrodes for CO_2 Reduction to CO, *Adv. Funct. Mater.*, 2022, **32**, 2111597.

5 J. Li, H. Zeng, X. Dong, Y. Ding, S. Hu, R. Zhang, Y. Dai, P. Cui, Z. Xiao, D. Zhao, L. Zhou, T. Zheng, J. Xiao, J. Zeng and C. Xia, Selective CO_2 electrolysis to CO using isolated antimony alloyed copper, *Nat. Commun.*, 2023, **14**, 340.

6 M. C. O. Monteiro, M. F. Philips, K. J. P. Schouten and M. T. M. Koper, Efficiency and selectivity of CO_2 reduction to CO on gold gas diffusion electrodes in acidic media, *Nat. Commun.*, 2021, **12**, 4943.

7 J. Y. T. Kim, C. Sellers, S. Hao, T. P. Senftle and H. Wang, Different distributions of multi-carbon products in CO_2 and CO electroreduction under practical reaction conditions, *Nat. Catal.*, 2023, **6**, 1115–1124.

8 M. Jouny, G. S. Hutchings and F. Jiao, Carbon monoxide electroreduction as an emerging platform for carbon utilization, *Nat. Catal.*, 2019, **2**, 1062–1070.

9 X. Wang, Y. Chen, F. Li, R. K. Miao, J. E. Huang, Z. Zhao, X.-Y. Li, R. Dorakhan, S. Chu, J. Wu, S. Zheng, W. Ni, D. Kim, S. Park, Y. Liang, A. Ozden, P. Ou, Y. Hou, D. Sinton and E. H. Sargent, Site-selective protonation enables efficient carbon monoxide electroreduction to acetate, *Nat. Commun.*, 2024, **15**, 616.

10 W. Deng, P. Zhang, Y. Qiao, G. Kastlunger, N. Govindarajan, A. Xu, I. Chorkendorff, B. Seger and J. Gong, Unraveling the rate-determining step of C_{2+} products during electrochemical CO reduction, *Nat. Commun.*, 2024, **15**, 892.

11 L. Wang, S. A. Nitopi, E. Bertheussen, M. Orazov, C. G. Morales-Guio, X. Liu, D. C. Higgins, K. Chan, J. K. Nørskov, C. Hahn and T. F. Jaramillo, Electrochemical Carbon Monoxide Reduction on Polycrystalline Copper: Effects of Potential, Pressure, and pH on Selectivity toward Multicarbon and Oxygenated Products, *ACS Catal.*, 2018, **8**, 7445–7454.

12 M. Jouny, W. Luc and F. Jiao, High-rate electroreduction of carbon monoxide to multi-carbon products, *Nat. Catal.*, 2018, **1**, 748–755.

13 W. Gao, Y. Xu, L. Fu, X. Chang and B. Xu, Experimental evidence of distinct sites for CO_2-to-CO and CO conversion on Cu in the electrochemical CO_2 reduction reaction, *Nat. Catal.*, 2023, **6**, 885–894.

14 Q. Sun, Y. Zhao, X. Tan, C. Jia, Z. Su, Q. Meyer, M. I. Ahmed and C. Zhao, Atomically Dispersed Cu–Au Alloy for Efficient Electrocatalytic Reduction of Carbon Monoxide to Acetate, *ACS Catal.*, 2023, **13**, 5689–5696.

15 Y. Ji, Z. Chen, R. Wei, C. Yang, Y. Wang, J. Xu, H. Zhang, A. Guan, J. Chen, T.-K. Sham, J. Luo, Y. Yang, X. Xu and G. Zheng, Selective CO-to-acetate electroreduction via intermediate adsorption tuning on ordered Cu–Pd sites, *Nat. Catal.*, 2022, **5**, 251–258.

16 H. Wang, J. Xue, C. Liu, Z. Chen, C. Li, X. Li, T. Zheng, Q. Jiang and C. Xia, CO_2 electrolysis toward acetate: a review, *Curr. Opin. Electrochem.*, 2023, **39**, 101253.

17 W. Luc, X. Fu, J. Shi, J.-J. Lv, M. Jouny, B. H. Ko, Y. Xu, Q. Tu, X. Hu, J. Wu, Q. Yue, Y. Liu, F. Jiao and Y. Kang, Two-dimensional copper nanosheets for electrochemical reduction of carbon monoxide to acetate, *Nat. Catal.*, 2019, **2**, 423–430.

18 K. P. Kuhl, E. R. Cave, D. N. Abram and T. F. Jaramillo, New insights into the electrochemical reduction of carbon dioxide on metallic copper surfaces, *Energy Environ. Sci.*, 2012, **5**, 7050–7059.

19 M. Ma, W. Deng, A. Xu, D. Hochfilzer, Y. Qiao, K. Chan, I. Chorkendorff and B. Seger, Local reaction environment for selective electroreduction of carbon monoxide, *Energy Environ. Sci.*, 2022, **15**, 2470–2478.

20 M. Jouny, J.-J. Lv, T. Cheng, B. H. Ko, J.-J. Zhu, W. A. Goddard and F. Jiao, Formation of carbon–nitrogen bonds in carbon monoxide electrolysis, *Nat. Chem.*, 2019, **11**, 846–851.

21 H. H. Heenen, H. Shin, G. Kastlunger, S. Overa, J. A. Gauthier, F. Jiao and K. Chan, The mechanism for acetate formation in electrochemical $CO_{(2)}$ reduction on Cu: selectivity with potential, pH, and nanostructuring, *Energy Environ. Sci.*, 2022, **15**, 3978–3990.

22 Z. Ma, Z. Yang, W. Lai, Q. Wang, Y. Qiao, H. Tao, C. Lian, M. Liu, C. Ma, A. Pan and H. Huang, CO_2 electroreduction to multicarbon products in strongly acidic electrolyte via synergistically modulating the local microenvironment, *Nat. Commun.*, 2022, **13**, 7596.

23 C. Chen, H. Jin, P. Wang, X. Sun, M. Jaroniec, Y. Zheng and S.-Z. Qiao, Local reaction environment in electrocatalysis, *Chem. Soc. Rev.*, 2024, **53**, 2022–2055.

24 C. W. Li, J. Ciston and M. W. Kanan, Electroreduction of carbon monoxide to liquid fuel on oxide-derived nanocrystalline copper, *Nature*, 2014, **508**, 504–507.

25 X. Bai, M. He, Y. Xu, B. Xu, Q. Lu, J. Wang and C. Ling, New Mechanistic Insights into CO_2/CO Electroreduction to Acetate by Combining Computations and Experiments, *ACS Catal.*, 2024, **14**, 3171–3180.

26 H. Ma, E. Ibáñez-Alé, F. You, N. López and B. S. Yeo, Electrochemical Formation of C_{2+} Products Steered by Bridge-Bonded *CO Confined by *OH Domains, *J. Am. Chem. Soc.*, 2024, **146**, 30183–30193.

27 G. Kresse and J. Hafner, Ab initio molecular-dynamics for liquid-metals, *Phys. Rev. B:Condens. Matter Mater. Phys.*, 1993, **47**, 558–561.

28 G. Kresse and J. Furthmuller, Efficiency of Ab-Initio Total Energy Calculations for Metals and Semiconductors Using a Plane-Wave Basis Set, *Comput. Mater. Sci.*, 1996, **6**, 15–50.

29 P. E. Blöchl, Projector augmented-wave method, *Phys. Rev. B:Condens. Matter Mater. Phys.*, 1994, **50**, 17953–17979.

30 G. Kresse and D. Joubert, From Ultrasoft Pseudopotentials to the Projector Augmented-Wave Method, *Phys. Rev. B:Condens. Matter Mater. Phys.*, 1999, **59**, 1758–1775.

31 J. P. Perdew, K. Burke and M. Ernzerhof, Generalized Gradient Approximation Made Simple, *Phys. Rev. Lett.*, 1996, **77**, 3865–3868.

32 S. Grimme, J. Antony, S. Ehrlich and H. Krieg, A consistent and accurate ab initio parametrization of density functional dispersion correction (DFT-D) for the 94 elements H-Pu, *J. Chem. Phys.*, 2010, **132**, 154104.

33 T. K. Woo, P. M. Margl, P. E. Blöchl and T. Ziegler, A Combined Car−Parrinello QM/MM Implementation for ab Initio Molecular Dynamics Simulations of Extended Systems: Application to Transition Metal Catalysis, *J. Phys. Chem. B*, 1997, **101**, 7877–7880.

34 C. Jarzynski, Nonequilibrium Equality for Free Energy Differences, *Phys. Rev. Lett.*, 1997, **78**, 2690–2693.

35 S. Yu, Z. Levell, Z. Jiang, X. Zhao and Y. Liu, What Is the Rate-Limiting Step of Oxygen Reduction Reaction on Fe–N–C Catalysts?, *J. Am. Chem. Soc.*, 2023, **145**, 25352–25356.

36 X. Zhao and Y. Liu, Origin of Selective Production of Hydrogen Peroxide by Electrochemical Oxygen Reduction, *J. Am. Chem. Soc.*, 2021, **143**, 9423–9428.

37 W. G. Hoover, Canonical dynamics: equilibrium phase-space distributions, *Phys. Rev. A*, 1985, **31**, 1695–1697.

38 Y. Lum, T. Cheng, W. A. Goddard III and J. W. Ager, Electrochemical CO Reduction Builds Solvent Water into Oxygenate Products, *J. Am. Chem. Soc.*, 2018, **140**, 9337–9340.

39 J. Jin, J. Wicks, Q. Min, J. Li, Y. Hu, J. Ma, Y. Wang, Z. Jiang, Y. Xu, R. Lu, G. Si, P. Papangelakis, M. Shakouri, Q. Xiao, P. Ou, X. Wang, Z. Chen, W. Zhang, K. Yu, J. Song, X. Jiang, P. Qiu, Y. Lou, D. Wu, Y. Mao, A. Ozden, C. Wang, B. Y. Xia, X. Hu, V. P. Dravid, Y.-M. Yiu, T.-K. Sham, Z. Wang, D. Sinton, L. Mai, E. H. Sargent and Y. Pang, Constrained C_2 adsorbate orientation enables CO-to-acetate electroreduction, *Nature*, 2023, **617**, 724–729.

40 X. Yan, M. Zhang, Y. Chen, Y. Wu, R. Wu, Q. Wan, C. Liu, T. Zheng, R. Feng, J. Zhang, C. Chen, C. Xia, Q. Zhu, X. Sun, Q. Qian and B. Han, Synergy of Cu/C_3N_4 Interface and Cu Nanoparticles Dual Catalytic Regions in Electrolysis of CO to Acetic Acid, *Angew. Chem., Int. Ed.*, 2023, **62**, e202301507.

41 R. A. DiStasio Jr, B. Santra, Z. Li, X. Wu and R. Car, The individual and collective effects of exact exchange and dispersion interactions on the ab initio structure of liquid water, *J. Chem. Phys.*, 2014, 141.

42 J. Daru, H. Forbert, J. Behler and D. Marx, Coupled Cluster Molecular Dynamics of Condensed Phase Systems Enabled by Machine Learning Potentials: Liquid Water Benchmark, *Phys. Rev. Lett.*, 2022, **129**, 226001.

43 P. E. Tiberti M, T. Bengtsen, W. Boomsma and K. Lindorff-Larsen, ENCORE: Software for Quantitative Ensemble Comparison, *PLoS Comput. Biol.*, 2015, **11**, e1004415.

44 N. M. Ofodum, Q. Qi, R. Chandradat, T. Warfle and X. Lu, Advancing Dynamic Polymer Mechanochemistry through Synergetic Conformational Gearing, *J. Am. Chem. Soc.*, 2024, **146**, 17700–17711.

45 S. Genheden, A. Reymer, P. Saenz-Méndez and L. A. Eriksson, in *Computational Tools for Chemical Biology*, ed. S. Martín-Santamaría, The Royal Society of Chemistry, 2017, ch.1, pp. 1–38.

46 M. Miciaccia, B. D. Belviso, M. Iaselli, G. Cingolani, S. Ferorelli, M. Cappellari, P. Loguercio Polosa, M. G. Perrone, R. Caliandro and A. Scilimati, Three-dimensional structure of human cyclooxygenase (*h*COX)-1, *Sci. Rep.*, 2021, **11**, 4312.

47 J. Hou, B. Xu and Q. Lu, Influence of electric double layer rigidity on CO adsorption and electroreduction rate, *Nat. Commun.*, 2024, **15**, 1926.

48 P. Li, Y. Jiao, Y. Ruan, H. Fei, Y. Men, C. Guo, Y. Wu and S. Chen, Revealing the role of double-layer microenvironments in pH-dependent oxygen reduction activity over metal-nitrogen-carbon catalysts, *Nat. Commun.*, 2023, **14**, 6936.

49 P. Habibi, A. Rahbari, S. Blazquez, C. Vega, P. Dey, T. J. H. Vlugt and O. A. Moultos, A New Force Field for OH– for Computing Thermodynamic and Transport Properties of H2 and O2 in Aqueous NaOH and KOH Solutions, *J. Phys. Chem. B*, 2022, **126**, 9376–9387.

50 T. Zhang, S. Xu, D.-L. Chen, T. Luo, J. Zhou, L. Kong, J. Feng, J.-Q. Lu, X. Weng, A.-J. Wang, Z. Li, Y. Su and F. Yang, Selective Increase in CO_2 Electroreduction to Ethanol Activity at Nanograin-Boundary-Rich Mixed Cu(I)/Cu(0) Sites via Enriching Co-Adsorbed CO and Hydroxyl Species, *Angew. Chem., Int. Ed.*, 2024, **63**, e202407748.